Transparent Nacre-like Composites Toughened through Mineral Bridges

Journal Article

Author(s):
Magrini, Tommaso; Moser, Simon; Fellner, Madeleine; Lauria, Alessandro; Bouville, Florian; Studart, André R.

Transparent Nacre-like Composites Toughened through Mineral Bridges

Tommaso Magrini, Simon Moser, Madeleine Fellner, Alessandro Lauria, Florian Bouville,* and André R. Studart*

Bulk materials with remarkable mechanical properties have been developed by incorporating design principles of biological nacre into synthetic composites. However, this potential has not yet been fully leveraged for the fabrication of tough and strong materials that are also optically transparent. In this work, a manufacturing route that enables the formation of nacre-like mineral bridges in a bioinspired composite consisting of glass platelets infiltrated with an index-matching polymer matrix is developed. By varying the pressure applied during compaction of the glass platelets, composites with tunable levels of mineral bridges and platelet interconnectivity can be easily fabricated. The effect of platelet interconnectivity on the mechanical strength and fracture behavior of the bioinspired composites is investigated by performing state-of-the-art fracture experiments combined with in situ electron microscopy. The results show that the formation of interconnections between platelets leads to bulk transparent materials with an unprecedented combination of strength and fracture toughness. This unusual set of properties can potentially fulfill currently unmet demands in electronic displays and related technologies.

1. Introduction

Strong and transparent materials are useful in a myriad of applications, from displays in electronic devices and fibers in

T. Magrini, S. Moser, Prof. A. R. Studart
Complex Materials
Department of Materials
ETH Zürich
Zürich 8093, Switzerland
E-mail: andre.studart@mat.ethz.ch
M. Fellner, Dr. A. Lauria
Multifunctional Materials
Department of Materials
ETH Zürich
Zürich 8093, Switzerland
Dr. F. Bouville
Centre for Advanced Structural Ceramics
Department of Materials
Imperial College London, South Kensington Campus
London SW7 2AZ, UK
E-mail: f.bouville@imperial.ac.uk

optical communication to structural elements in construction, architecture, and arts. In spite of this broad demand, high strength and optical transparency are properties that are usually difficult to reconcile in single homogeneous materials. This explains the widespread use of silica-based glass as a dominant material in applications where strength and transparency are simultaneously required. While state-of-the-art oxide glasses are sufficiently strong to withstand the mechanical loading conditions developed in several application scenarios, this material is not able to resist crack propagation and thus fractures in a brittle and catastrophic manner. Therefore, materials combining strength, toughness, and transparency are of high practical and technological relevance.

Composite materials have long been exploited to implement multiple functionalities in bulk parts that cannot be achieved using single material classes. In particular, biological composites, such as bone, wood, and mollusk shells are striking examples of how building blocks with rather weak intrinsic properties can be assembled into hierarchical structures with multiple unique functionalities.[1–4] The nacreous layer of mollusk shells is one of the most prominent examples of a biological composite that is simultaneous stiff and tough, despite the weak nature of its constituent building blocks.[5,6] These properties arise from the organization of stiff calcium carbonate platelets and a soft biopolymer matrix into a so-called brick-and-mortar structure. Some of the key structural features of such a brick-and-mortar architecture include the staggered arrangement of platelets,[5,7] the energy-dissipative nature of the biopolymer matrix,[8] as well as the nanogranular structure,[9] the surface asperities, the interlocking geometry,[7,10,11] and the interconnectivity between the platelets.[2]

Several manufacturing routes have been proposed to emulate the design principles of nacre in synthetic composite materials.[12–17] Methods that allow for the formation of highly-aligned platelets that are interconnected by stiff mineral bridges have been shown to be very effective in simultaneously enhancing the fracture strength and toughness of nacre-like composites.[18–21] In one of these approaches, mineral bridges are created by the dewetting of a titania coating from the surface of alumina platelets during sintering of magnetically aligned scaffolds.[20] The formation of mineral bridges has also been achieved through the incorporation of specific chemicals

into the particle suspensions used to produce nacre-like structures by the ice-templating technique.[18,21] Additive manufacturing technologies have also been utilized to fabricate all-polymer nacre-like structures with tunable interconnectivity between bricks.[22] While the importance of mineral bridges has been demonstrated in several experimental and computational studies,[23,24] the strengthening potential of this structural feature has not yet been harnessed for the development of transparent nacre-like materials.[25]

Here, we report a simple approach to fabricate transparent nacre-like composites that are strengthened and toughened through the formation of interplatelet mineral bridges. Composites with a nacre-like architecture are manufactured using glass platelets aligned and interconnected at random contact points in an index-matching polymer phase. First, we describe the processing steps involved in the manufacturing of such bioinspired structures with tunable platelet interconnectivity and quantify the level of interconnectivity using image analysis protocols. The mechanical and toughening behavior of composites with distinct interconnectivity levels is then investigated by performing controlled fracture experiments. Finally, the optical properties of the nacre-like composites are evaluated and analyzed in the context of display applications.

2. Results and Discussion

Transparent nacre-like composites are fabricated by a multistep process involving well-established manufacturing technologies (**Figure 1**a). First, glass flakes with typical diameter of 300 µm and thickness of 1 µm are suspended in water and assembled into thick discs through vacuum-assisted filtration. The resulting discs are densified by uniaxial compaction at room temperature under compressive stresses in the range 5–110 MPa. Compressed compacts are then sintered at 600 °C in a conventional oven to form mineral bridges between adjacent flakes. Finally, the sintered scaffolds are infiltrated with a mixture of monomers and initiator to generate a solid organic matrix upon polymerization. A monomer mixture comprising poly(methyl methacrylate) and phenanthrene is utilized to form an organic matrix with refractive index that matches that of the glass flakes. This ensures the formation of a nacre-like architecture that is optically transparent in spite of the high density of platelet-matrix interfaces.

The manufacturing process determines the microstructural features of the resulting nacre-like composites. While the uniaxial compression step leads to a high density of well-aligned glass platelets, the sintering procedure enables the formation of stiff interconnections between such platelets. Our experiments show that the interconnectivity between the glass platelets can be enhanced by increasing the pressure applied during compression. Importantly, such an increase in interconnectivity occurs while maintaining the relative density of glass phase at comparable levels within the range 55–62% (Figure 1b). This observation indicates that the system has reached the maximum packing density of platelets. Although maximum packing is achieved at the global level, higher compression stresses presumably favor the formation of stronger contact points between the platelets, which ultimately result in mineral interconnections after sintering.

To establish a direct correlation between the compressive stress applied during compaction and the interconnectivity of the sintered nacre-like architecture, we performed image analysis on polished composite specimens subjected to compaction pressures between 5 and 110 MPa (Figure 1c,d). In this analysis, the level of interconnectivity is quantified through measurements of the characteristic feature sizes of the microstructure. The characteristic features of interest are the individual platelets (1 µm) and the adjacent platelets that are sufficiently close to form a cluster (> 1 µm). Such analysis reveals that the distribution of cluster sizes moves toward coarser length scales, if the specimen is subjected to higher compressive stresses during compaction (Figure 1c). This effect is quantified by normalizing the number of counts of a given cluster relative to the number of counts of individual platelets, which eventually leads to a relative measure of the frequency of clusters of a specific size, $f(\delta)$ (Figure 1e). Our results show that an increase in compressive stress from 5 to 110 MPa increases the maximum cluster size from 4 to around 8 µm. Clusters containing 2–3 platelets are particularly evident in specimens compressed above 20 MPa. For the highest stress of 110 MPa, the relative frequency of these clusters is three to fivefold higher compared to samples pressed at 5 MPa (Figure 1e).

Whereas the relative frequency of clusters captures the formation of strong contact points between platelets during sintering, the overall interconnectivity of the solid phase throughout the material is a more appropriate microstructural parameter to be correlated with the mechanical properties of the composite. We quantify the overall interconnectivity of the structure, χ, by measuring the number of counts of clusters (of all sizes) relative to the total number of all counts of solid phase (clusters and individual platelets). Because this image analysis protocol also leads to a finite interconnectivity value for nonsintered specimens without strong platelet contacts (χ_0), we normalize the χ values of the sintered samples by those of the nonsintered counterparts (χ/χ_0) and hypothesize that this structural parameter should correlate directly with the mechanical properties of the nacre-like composites. In agreement with our earlier qualitative analysis of the microstructures, the χ/χ_0 value of our composites was found to increase from 0.43 to 1.13 by increasing the compressive stress from 5 to 110 (Figure 1f).

The effect of the platelet interconnectivity on the mechanical behavior of nacre-like composites was evaluated by performing three-point bending tests on notched and un-notched specimens prepared at distinct compressive stresses (**Figure 2**a,b). Tests on un-notched samples were used to measure the flexural strength and elastic modulus of the composites, whereas experiments with notched specimens provided information about the resistance of the material against crack initiation (K_{IC}) and propagation (K_{IJ}).

Increasing the platelet interconnectivity (χ/χ_0) from 0.43 to 1.13 was found to enhance the flexural strength and elastic modulus of the transparent nacre-like composites by a factor of 2 and 4, respectively, without sacrificing their fracture toughness. The dependence of strength and modulus on the platelet interconnectivity shows a similar trend to that observed in our previous study on nacre-like composites containing alumina platelets interconnected via titania mineral bridges.[26] In this earlier work, the level of interconnectivity was quantified
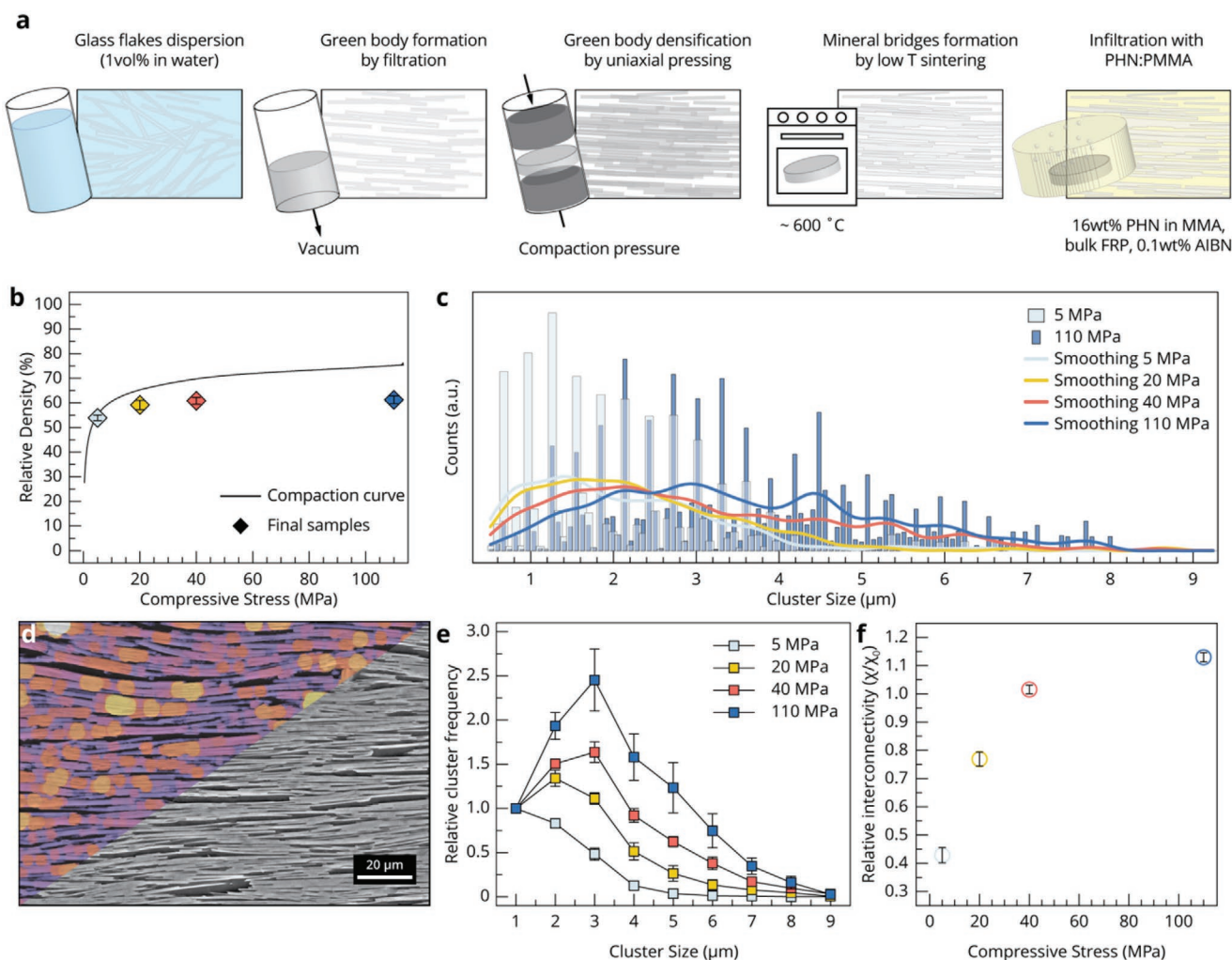
Figure 1. Fabrication and microstructural features of the transparent nacre-like composites. a) Chart depicting the fabrication steps of the transparent nacre-like composites. b) Evolution of the relative density of flakes as a function of the pressure applied during compaction (solid black line). The final relative density after sintering of the samples is also shown (symbols). Gray, yellow, orange, and blue symbols correspond to the specimens that were subjected to compressive stresses of 5, 20, 40, and 110 MPa, respectively. c) Histogram illustrating the distribution of the cluster sizes in a specimen compacted at 5 MPa (wide gray bins), and at 110 MPa (narrow blue bins). The solid lines represent the smoothing of the cluster size distributions measured for each compaction pressure. d) (Bottom right) Scanning electron micrograph of a specimen compacted at 40 MPa. (Upper left) Superimposition of the color-coded spatial distribution of clusters on the SEM image. Purple features correspond to 1 µm clusters, whereas yellow features correspond to 6 µm clusters. e) Relative frequency of cluster sizes observed in samples prepared under different compaction pressures. The frequency is given by the ratio between the frequency of a given cluster larger than 1 µm and the frequency of 1 µm thick unconnected platelets. f) Relative interconnectivity (defined as χ/χ_0) of the final samples as a function of compressive stresses ranging from 5 up to 110 MPa. The gray, yellow, orange, and blue symbols correspond to relative interconnectivity values of 0.43, 0.77, 1.02, and 1.13, respectively.

by estimating the relative fraction of titania contacts between platelets using image analysis. Despite the different analytical protocols employed, the resulting interconnectivity parameters are expected to capture the same microstructural feature of the brick-and-mortar structures, namely the relative density of mineral bridges. Theoretical analysis using a simplified shear lag model suggests that the strength and elastic modulus of nacre-like composites should increase linearly with the relative fraction of mineral bridges.[26] The strength and modulus data obtained in this work seem to follow this trend (Figure 2c), providing further experimental evidence of the analytical prediction. Although the mineral bridges are the major structural features controlling the composite fracture strength, previous

work[27] suggests that the polymer phase itself also plays an important role in transferring stress away from the scaffolds, thus increasing the strength without compromising toughness.

The resistance of the composites against crack initiation and growth was quantified by measuring force-displacement curves for single-edge notched beam (SENB) specimens featuring varying levels of platelet interconnectivity (Figure 2b). In these experiments, mechanical load was applied normal to the platelet long axis to induce crack propagation perpendicular to the platelet's basal plane. The experimental results show that all composites exhibit graceful (non-catastrophic) failure, regardless of their interconnectivity. This suggests that the propagation of the main crack initiated close to the notch
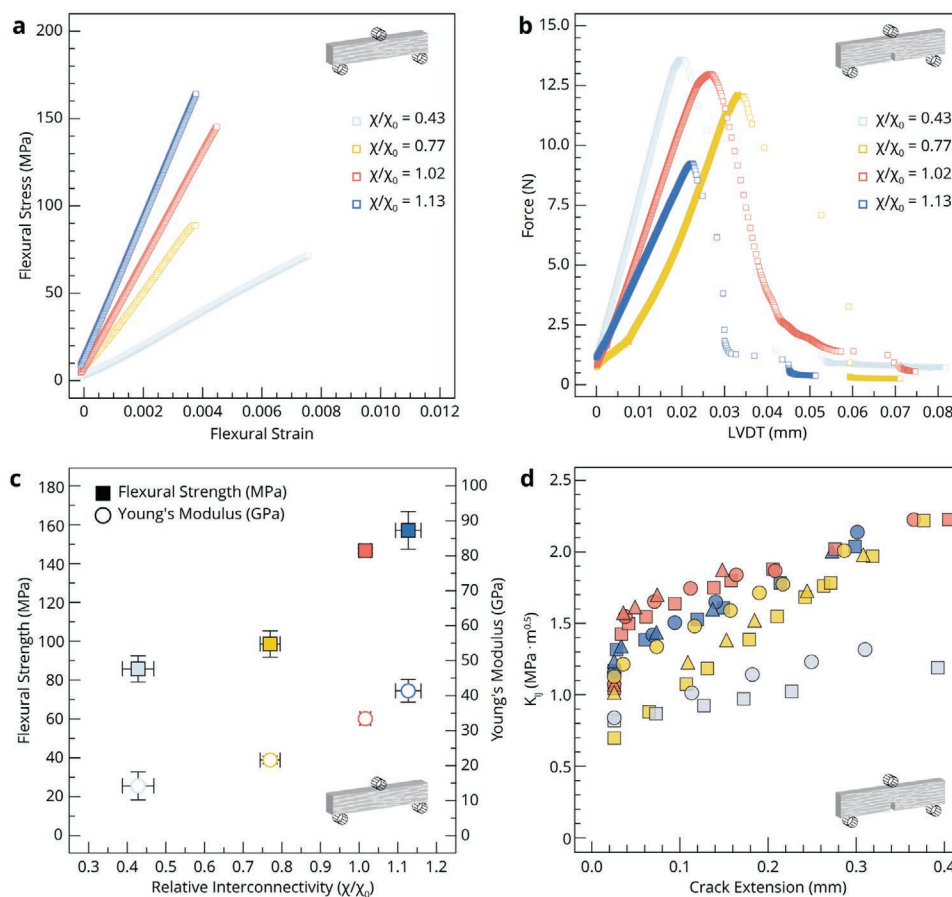
**ADVANCED
SCIENCE NEWS**
www.advancedsciencenews.com

**ADVANCED
FUNCTIONAL
MATERIALS**
www.afm-journal.de

Figure 2. Flexural mechanical properties and crack growth resistance of the transparent nacre-like composites. a) Flexural stress as function of flexural strain for transparent nacre-like composite specimens prepared at different compaction pressures. Specimens prepared at 5, 20, 40, and 110 MPa display relative interconnectivity of 0.43, 0.77, 1.02, and 1.13, respectively. b) Force-displacement curves obtained from single edge notched bending (SENB) experiments on composites with distinct relative interconnectivities. c) Flexural strength (in MPa) and Young's modulus (in GPa) of the composites as a function of the relative interconnectivity. The error bars are representative of the measured standard deviation. d) Crack growth resistance (K_{IJ}) as a function of crack extension (Δa) for the different nacre-like composites subjected to SENB fracture experiments.

is hindered by toughening mechanisms within the nacre-like microstructure. Such toughening effect was quantified by calculating the resistance imposed by the material against crack growth as a function of the extension of the crack, also called the R-curve.

All the investigated nacre-like composites exhibit a rising R-curve behavior, which is a typical signature of toughened materials (Figure 2d). The fracture toughness of the composites was quantified through the stress intensity factor, K. Specimens with high platelet interconnectivity ($\chi/\chi_0 = 1.02$ and 1.13) showed fracture toughness of ≈2 MPa m$^{1/2}$ for a relatively small crack extension of 400 μm. The K values of such composites were found to increase sharply at the onset of cracking before reaching a state of steady but gradual increase as the crack is further extended. The sharp initial increase in fracture toughness might be related to heterogeneities in the composite microstructure or inaccuracies in the measurement at very small crack extensions. Importantly, the high toughness level reached in the steady part of the R-curve reflects the presence of a strong interconnected network of platelets in composites with high χ/χ_0 values. In contrast to these strongly toughened

microstructures, composites with the lowest platelet interconnectivity ($\chi/\chi_0 = 0.43$) show only the steady and gradual increase of K as a function of crack extension. This is probably caused by the lower strength and stiffness of the platelet network within these composites. Specimens with intermediate interconnectivity ($\chi/\chi_0 = 0.77$) exhibit fracture toughness values that lie in between the two R-curve profiles discussed above. Interestingly, the gain in fracture toughness in the steady and gradual part of the R-curve is comparable for all samples, suggesting the presence of the same toughening mechanisms within this crack extension range.

To gain more insights into the toughening mechanisms underlying the observed rising R-curve behavior, we conducted another series of fracture experiments using the wedge splitting test (WST) configuration (**Figure 3**). Such configuration allows for a stable growth of cracks through the controlled displacement of a wedge positioned on top of the sample notch. The propagation of the crack from the notch through the nacre-like microstructure was tracked by scanning electron micrograph (SEM) imaging of the cross-section of the composite during and after the fracture process.
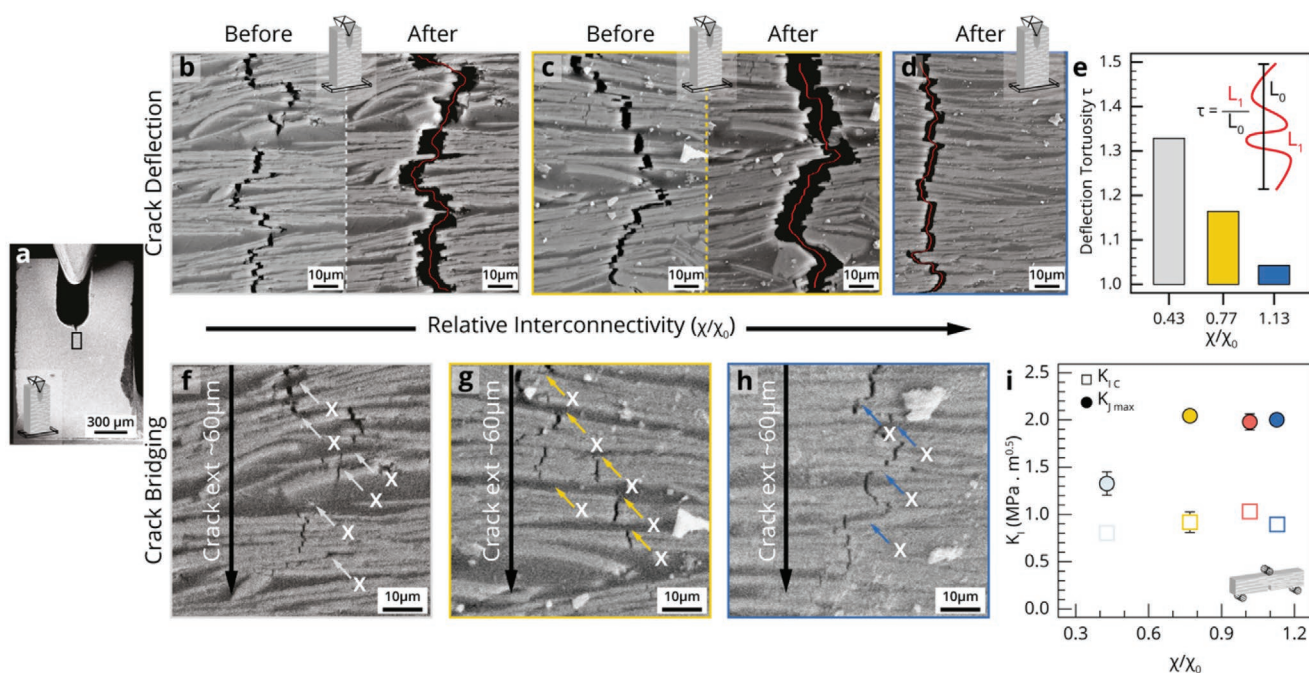
Figure 3. Fracture behavior of the transparent nacre-like composites. a) Scanning electron (SE) micrograph showing fracture of a specimen in a wedge-splitting-test (WST) configuration. b–d) Representative SE micrographs displaying the tortuous path of cracks at the beginning and toward the end of fracture experiments on specimens with relative interconnectivity of 0.43 (gray), 0.77 (yellow), and 1.13 (blue), respectively. The red line in each image represents the shortest crack path obtained by skeletonization of the two crack surfaces. e) Crack tortuosity (τ) resulting from deflection events in composites with different levels of interconnectivity (χ/χ_0). The tortuosity values correspond to the ratio between the total crack length (approximated by the red line shown in the micrograph) and the size of each frame along the direction of the crack. f–h) SE micrographs highlighting the presence of several polymer bridging locations during the propagation of the main crack. i) Critical stress intensity factors for crack initiation (K_{IC}) (empty symbols) and crack propagation $K_{I \, J\max}$ (filled symbols) measured in SENB specimens. The error bars indicate the measured standard deviation.

Several microscale fracture phenomena were observed during the stable crack growth experiments. First, platelet fracture appears to be the dominant failure mechanism in all the studied composites. This experimental finding is in line with theoretical estimates based on the aspect ratio (s) of the glass platelets and the shear strength (τ_y) of the poly(methyl methacrylate) (PMMA) matrix used for the fabrication of the nacre-like structures. Assuming that the yield shear strength of the polymer matrix to be lower than the strength of the platelet-matrix interface, a simplified shear lag model predicts that platelet fracture occurs if the platelet aspect ratio, s, is larger than a critical value, s_c.[28] In this simplified analysis, the critical aspect ratio is given by: $s_c = \sigma_f / \tau_y$, where σ_f is the tensile strength of the platelets. Taking $\sigma_f = 500$ MPa and $\tau_y = 20$ MPa as reasonable assumptions for, respectively, the tensile strength of the glass platelets and the shear strength of the PMMA matrix, one should expect s_c to be approximately equal to 25 for our composites. This s_c value is one order of magnitude smaller than the actual aspect ratio of the glass platelets ($s = 300$), which explains our experimental observation of platelet fracture as the dominant failure mode.

The second distinct feature revealed by the controlled fracture experiments is the local deflection of the main crack by the glass platelets as it propagates through the brick-and-mortar structure (Figure 3b,d). The extent of crack deflection in each of the investigated specimens was quantified by measuring the tortuosity of the crack using image analysis (see Videos S1 and S2

in the Supporting Information). Surprisingly, decreasing the platelet interconnectivity from 1.13 to 0.43 was found to increase the tortuosity of the crack by ≈25% (Figure 3e). This experimental observation suggests that the glass–glass interconnections work as obstacles against further propagation of the deflected cracks along the transverse direction, thus decreasing the tortuosity of the crack path. Theoretical analysis has shown that a crack deflection event is expected to reduce the stress intensity factor at the crack tip by a factor of ≈2 for a strong deflection angle of 90°.[29,30] This reduction in stress concentration becomes more pronounced for higher relative lengths of the kink generated upon crack deflection. Since the stronger crack deflection events observed in samples with lower platelet interconnectivity do not translate into a steeper R-curve response, other toughening mechanisms must dominate the crack propagation behavior of the studied composites.

Image analysis of the wake of the main crack shows that polymer bridges between the fractured surfaces is the third prominent microstructural feature of the fracture process (Figure 3f–h). Numerous unbroken polymer ligaments were found in the crack wake of all samples, regardless of the initial level of platelet interconnectivity. By bridging the fractured surfaces behind the main crack tip, such unbroken ligaments exert a closure force that resists crack opening, thus toughening the material. This toughening effect is proportional to the areal fraction of unbroken ligaments and depends on the deformation response of the polymer. Because all specimens

**ADVANCED
SCIENCE NEWS**
www.advancedsciencenews.com

**ADVANCED
FUNCTIONAL
MATERIALS**
www.afm-journal.de

contain the same polymer at comparable volume fraction, the fracture toughness amplification resulting from unbroken ligaments should not depend on the platelet interconnectivity. This interpretation is supported by the R-curve measurements, which indicate a comparable gain in the fracture toughness of all materials in the steady part of the curve (Figure 2d). Therefore, our results suggest that polymer bridging is the prevalent mechanism responsible for the increasing resistance of the nacre-like structures against crack propagation, whereas the toughness against crack initiation (K_{IC}) is controlled by the strength of the interconnected network of platelets.

The rising resistance against crack propagation is a unique feature of our bioinspired composite in comparison to other stiff and transparent materials. To illustrate this key advantage, we incorporate the mechanical data obtained for the nacre-like composites in an Ashby plot displaying the fracture toughness as a function of the fracture strength of other transparent structural materials (**Figure 4**a). The comparative analysis shows that nacre-like composites with platelet interconnectivity

reach maximum fracture toughness levels ($K_{IJ,max}$) that are ≈3 times higher than that of state-of-the-art silica glass and chemically-strengthened glasses used in display applications. Such toughening behavior prevents the shattering and brittle fracture typical of structural materials based on silica glass. Importantly, the high maximum toughness achieved is combined with a two-fold increase in the fracture strength of the composite in comparison to our previously reported nacre-like transparent material. This strengthening effect arises from the incorporation of mineral bridges between the glass platelets. By reconciling high fracture strength and rising crack growth resistance, the obtained glass-based composites achieve a set of antagonistic properties that is often challenging to attain in engineering structural materials.[31]

While the nacre-inspired microstructure of the composites is crucial to enhance mechanical performance, the presence of two distinct phases requires close matching of their refractive indices to ensure the high optical transparency desired in display and related applications. To evaluate the optical quality
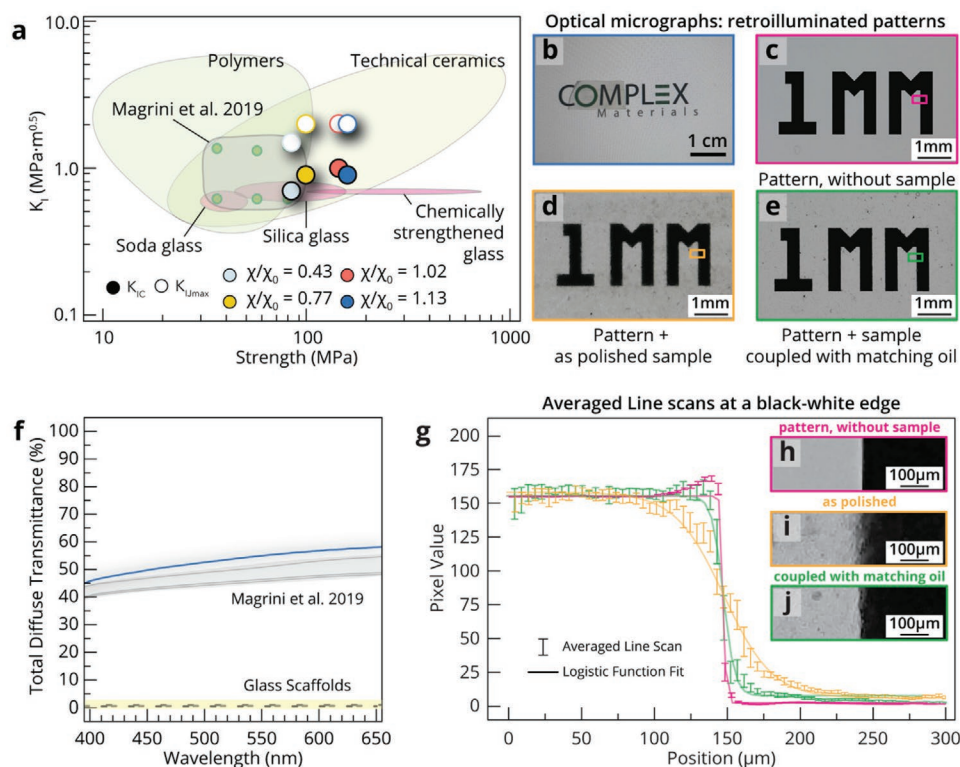

Figure 4. Optical properties of the transparent nacre-like composites. a) Ashby plot displaying the fracture toughness against the strength of different classes of transparent materials. The transparent composites reported in this work are highlighted and compared with state-of-the-art soda-lime glass, silica glass, and chemically-toughened glass. The measured values for the transparent nacre-like composites with relative interconnectivity (χ/χ_0) of 0.44, 0.77, 1.02, and 1.13 are indicated by the gray, yellow, orange, and blue symbols, respectively. Filled circles represent the measured K_{IC} data, whereas the $K_{IJ\,max}$ values are indicated by empty circles. Adapted from ref.[40] b) Photograph of a 0.7 mm thick sample with $\chi/\chi_0 = 1.13$ placed on top of a retroilluminated laptop screen. c–e) Photographs highlighting the optical translucency of the nacre-like composite with a refractive index matching oil e), compared to a sample without the oil d). A reference image taken without a sample on top of the pattern is shown in (c). f) Total diffuse transmittance of a nacre-like composite with relative interconnectivity of 1.13 (solid blue line) in comparison to the transmittance data of the previously-reported nacre-like samples with low density of mineral bridges (gray lines, gray-shaded area).[25] The optical transmittance of not-infiltrated glass scaffolds are also indicated (dashed gray lines, yellow-shaded area).[25] g) Averaged line scans showing the pixel brightness across sharp white-to-black transitions on patterns without any sample (pink symbols), with an as-polished sample (orange symbols), and without a sample coupled with a refractive index matching immersion oil (green symbols). The error bars indicate the measured standard deviation. The solid lines represent logistic functions fitted to each experimental line scan. h–j) Images of the areas employed to measure the pixel brightness over a white-to-black transition for patterns without any sample h), with an as-polished sample i), and with a sample optically coupled with an index matching oil j).

**ADVANCED
SCIENCE NEWS**

www.advancedsciencenews.com

**ADVANCED
FUNCTIONAL
MATERIALS**

www.afm-journal.de

achieved in composites prepared with a mixture of poly(methyl methacrylate) and phenanthrene as index-matching organic phase, we measured the optical transmittance of the composites and the sharpness of retro-illuminated patterns covered with the composite (Figure 4b,j). The optical measurements show that the presence of the index-matching organic phase enables significant light transmission through an otherwise opaque scaffold. The transmittance level achieved within the visible wavelength range is comparable to that previously reported for glass-reinforced nacre-like composites without mineral bridges (Figure 4f). This demonstrates that the incorporation of interconnections between the platelets improves the fracture strength of the composite significantly without sacrificing the transparency of the material. In fact, optical measurements on composites with distinct χ/χ_0 values reveal that a 1.5-fold increase in platelet interconnectivity enhances up to 10% the total diffuse transmittance of the material (Figure S1, Supporting Information). This effect could arise from the fact that part of the platelet-matrix interface is replaced by glass–glass connections in composites with higher χ/χ_0 levels. Since defects and air inclusions are often associated with the platelet-matrix interfaces, the partial replacement of these by glass–glass contacts reduces the density of potential scattering sites, thus increasing the diffuse transmittance of the composites.[25]

The optical transmittance achieved is quite high in view of the high concentration of platelet-matrix interfaces present in the material. Since perfect index-matching conditions cannot be reached experimentally across the whole visible wavelength range and each platelet-matrix interface potentially hosts scattering defects or air inclusions, these materials transmit light by diffuse scattering. This is manifested by a strong hazing effect if a composite specimen is positioned between the observer and a retro-illuminated pattern. To reduce undesired hazing and thus ensure the formation of sharp images in display applications, it is important to position the material close to the light source and to minimize scattering at the surface of the composite. Surface scattering can be minimized using a refractive index-matching phase between the sample and the pattern (Figure 4b–e). We illustrate the level of image sharpness that can be attained with this approach by using an immersion oil as index-matching phase between a surface-polished sample and a retro-illuminated pattern (Figure 4e). Sharpness was assessed by measuring the brightness of individual pixels as one moves across a black-white border of the pattern (Figure 4g–j). Fitting a logistic function to the obtained experimental data allows us to quantify the level of sharpness using the steepness parameter, κ (see Equation (11)). Our analysis reveals that the sharpness (κ) of the polished specimen can be improved by 7 times using a refractive index-matching oil. This condition can potentially also be fulfilled by utilizing commercially-available silicones instead of oil as the index-matching medium.[32–34] Such experimental demonstration highlights the direct applicability of the investigated composites in display applications.

3. Conclusions

Bulk composites combining high toughness, strength, and optical transparency can be fabricated by creating a nacre-inspired architecture comprising interconnected glass platelets infiltrated with an index-matching polymer matrix. The interconnected reinforcing phase is obtained through a series of simple processing steps, involving vacuum filtration, uniaxial pressing, and sintering protocols. Platelet interconnectivity can be tuned by varying the pressure applied during uniaxial compaction. Strong interconnections are generated at the contact points between the pressed platelets during sintering. Increasing the platelet interconnectivity significantly enhances the mechanical strength and initial fracture toughness of the transparent nacre-like composites. Besides this strengthening effect, the composites also exhibit rising resistance against crack growth. The increasing crack growth resistance of the composite probably arises from polymer bridges formed in the wake of the main crack and seems independent from the level of interconnectivity of the platelets. Nacre-like composites with highly interconnected platelets are two times stronger and 20% tougher than counterparts with low density of mineral bridges. Such mechanical improvement is achieved without compromising the optical transparency of the composite. The sharp contrast observed in a retro-illuminated pattern covered with the composite demonstrates the potential of this material as a tough and strong alternative to state-of-the-art brittle displays.

4. Experimental Section

Composite Fabrication: Transparent nacre-like composites were fabricated using a previously reported process.[25] In this procedure, 5.2 g of commercially available glass microplatelets (ECR GlassFlake, GF100M, Glassflake LTD, England) were suspended in 200 mL of double deionized (DI) water, leading to a 1% v/v suspension. The suspension was cast into a laboratory filtration setup equipped with a Plexiglas tube to accommodate up to 100 mL of liquid. The tube has an inner diameter of 30 mm. The large size of the glass microplatelets (≈300 aspect ratio, 1 µm thickness) allowed them to deposit within 15–20 min and stack on their base plane, parallel to each other. As the supernatant became optically clear, vacuum was gently pulled and the excess water was removed. It is therefore possible to collect the glass platelets at the bottom of the setup to generate a green body. The green body was then transferred to a steel mold (31 mm diameter) and uniaxially pressed. The compaction was performed at room temperature in a mechanical testing machine (Instron, USA) by applying forces that range from 1 kN to 80 kN at a displacement rate of 0.5 mm min⁻¹. Finally, the compacted green body was transferred into a furnace (Nabertherm GmbH, Germany) for sintering at 575–600 °C for 90 min with a 1 °C min⁻¹ heating rate. The nacre-like glass scaffold was then functionalized with 3-(trimethoxysilyl)propyl methacrylate (Sigma-Aldrich GmbH, Germany), following already reported procedures.[25,27,35] The functionalized scaffold was infiltrated with a monomer mixture that is polymerized into a refractive index matching polymer. For this purpose, a monomer mixture of methyl methacrylate (MMA, Acros Organics GmbH, Germany), 2′-azobis (2–methylpropionitrile) (AIBN, Sigma-Aldrich GmbH, Germany) and phenanthrene (PHN, abcr GmbH, Germany) at a MMA:AIBN:PHN weight ratio of 1.00:0.001:0.16 was chosen. The bulk free radical polymerization was carried out at 60 °C in an oil bath for 12–14 h under nitrogen atmosphere. The polymerized parts were then postcured in an oven (Thermo Fisher Scientific, USA) at 100 °C under nitrogen atmosphere. The excess resin was finally removed using a rotating polishing machine (Struers GmbH, Germany), before cutting and testing the infiltrated composite.

Microstructural Analysis: Quantification of the microstructural features of the transparent nacre-like composites was performed by image analysis of SEM cross sections. First, the cross sections of the

**ADVANCED
SCIENCE NEWS**

www.advancedsciencenews.com

**ADVANCED
FUNCTIONAL
MATERIALS**

www.afm-journal.de

composites were manually polished using up to the 4000 grit polishing paper, and then mirror polished using a clothed paper in combination with colloidal suspensions with sizes ranging from 9 μm down to 1 μm. In order to ensure the same surface finish on all the different specimens, the cross sections were polished using a Broad Ion Beam (IM4000, Hitachi, Japan). Before SEM imaging, the samples were sputtered with a 6 nm layer of Pt. SEM imaging was performed using the secondary electron detector (SE detector) at an acceleration voltage of 15 kV (Leo 1530, Zeiss GmbH, Germany). Up to 30 images per sample were acquired and analyzed using the open source image analysis software Fiji.[36] First, a threshold was applied to separate the grayscale value between the platelets and the polymeric matrix and thus obtain binary images. The platelets areal fraction and their interconnectivity were measured on the binary images by analyzing the histogram of each image and by using the plugin "local thickness," respectively. The output of the interconnectivity measurement is a thickness distribution, which sorts the 1 μm thick individual platelets and their assembly into clusters. The fraction of features at a certain integer cluster dimension (i μm) was expressed by the sum of each feature count registered between i ± 0.5 μm normalized by the total counts of 1 μm features. The latter represents the platelets that are not connected.

Mechanical Properties: The mechanical properties of the transparent nacre-like composites were characterized through flexural tests. Beams of 15 mm × 2 mm × 1.3 mm (length × width × thickness) were cut using a diamond saw (Struers GmbH, Germany) and subjected to three-point bending tests in a setup with a span of 12 mm. Prior to the test, the surface in tension was mirror polished and the edges subjected to tension were beveled using a 4000 grit polishing paper. The tests were performed using a universal mechanical testing machine (AGS-X mechanical tester, Shimadzu Ltd., Japan) at a displacement rate of 1 μm s^{-1}. The flexural stress σ_f and the flexural strain ε_f were calculated using Equations (1) and (2)

$$\sigma_f = \frac{3FL}{2bd^2} \tag{1}$$

$$\varepsilon_f = \frac{6Dd}{L^2} \tag{2}$$

where L, b, d are the support span, the sample width and the sample thickness, respectively, whereas F is the force and D is the bending deflection.

For the SENB tests, beams of 15 mm × 1.5 mm × 3 mm (length × width × thickness) were cut using a diamond saw (Struers GmbH, Germany). Notches with a 300 μm radius were produced using a wire saw (Well S.A., Switzerland) and sharpened manually using a razor blade. The total notch length was set between 40% and 45% of the total specimen depth (0.4–0.45 d). The SENB tests were carried out in a universal mechanical testing machine (AGS-X mechanical tester, Shimadzu Ltd., Japan) using a 12 mm span setup at a displacement rate of 1 μm s^{-1}. Crack propagation was recorded using a 2.3 Mpx camera. From the recorded videos, the position of the crack tip and the total crack length were measured using Fiji,[36] with an accuracy of 8–10 μm. The overall straight trajectory of the crack across the sample depth (mode I) enables the use of standard fracture mechanics to calculate the energy dissipated during fracture (*J*-integral) as a function of the crack length (*a*).

The *J*-integral can be expressed as the sum of a plastic (J_{PL}) and an elastic (J_{EL}) contribution (Equation (3))

$$J = J_{PL} + J_{EL} \tag{3}$$

The elastic part of the *J*-integral can be expressed as (Equation (4))

$$J_{EL} = \frac{K_I^2}{E'} \tag{4}$$

where K_I is the stress intensity factor in fracture mode I and E' is the elastic modulus of the material subjected to plain strain.[37]

The stress intensity factor K_I can be calculated for different crack extensions (Δa) from the load (P) applied during a SENB test using the function $f\left(\frac{a}{w}\right)$, which is a geometric dimensionless function that solely depends on the ratio between the notch length (*a*) and the total specimen thickness (*w*). The stress intensity factor is finally obtained using the following expression (Equation (5))

$$K_I = \frac{P \cdot s}{b \cdot w^{1.5}} f\left(\frac{a}{w}\right) \tag{5}$$

where $f\left(\frac{a}{w}\right)$ is given by Equation (6)

$$f\left(\frac{a}{w}\right) = \frac{3 \cdot \left(\frac{a}{w}\right)^{0.5} \cdot \left[1.99 - \left(\frac{a}{w}\right) \cdot \left(1 - \frac{a}{w}\right) \cdot 2.15 - 3.93 \cdot \left(\frac{a}{w}\right) + 2.7 \cdot \left(\frac{a}{w}\right)^2\right]}{2 \cdot \left(1 + 2 \cdot \frac{a}{w}\right) \cdot \left(1 - \frac{a}{w}\right)^{1.5}} \tag{6}$$

The plastic part of the *J*-integral can be expressed as (Equation (7))

$$J_{PL} = \frac{1.9 \cdot A^{PL}}{\gamma \cdot b} \tag{7}$$

with A^{PL} and γ being the plastic area under the load-displacement curve and the unbroken ligament length, respectively. As γ decreases during the propagation of the main crack, A^{PL} can be obtained by Equation (8)

$$J_{PL\,n} = \left[J_{PL\,n-1} + \left(\frac{1.9}{\gamma_{n-1}}\right) \cdot \left(\frac{A_n^{PL} - A_{n-1}^{PL}}{b}\right)\right] \cdot \left[1 - \frac{a_n - a_{n-1}}{\gamma_{n-1}}\right] \tag{8}$$

After determination of both the elastic and the plastic contributions to the *J*-integral, the stress intensity factor during crack propagation (K_{IJ}) is calculated using Equation (9)

$$K_{IJ} = \sqrt{(J_{PL} + J_{EL}) \cdot E} \tag{9}$$

Fracture Visualization: WST performed inside the SEM enabled the direct visualization of the crack propagation through the microstructure of the composites. For these tests, specimens of dimensions 3.5 mm × 1 mm × 2 mm (height × width × depth) were cut and prenotched using a wire saw (Well S.A., Switzerland). The notch was sharpened manually using a razor blade until it reached up to 40% of the total specimen thickness. A custom-made wedge (≈45°) was manufactured and mounted on a microtester (2 kN tensile compression and horizontal bending stage, Deben, UK), that can be installed into a SEM for in situ measurements. Prior to testing, the WST specimens were sputtered with a Pt layer with thickness up to 6 nm. Before loading the setup into the SEM for testing, the specimens were positioned by engaging the tester's wedge into the notch at a displacement rate of 0.3 mm min^{-1}. The engage load of 1 N was kept on the specimen as the tester was installed into the SEM and the chamber was evacuated. The SEM was then operated in dual magnification mode, enabling video recording of the fracture at the large scale (≈imaging width 4 mm) and local scale (≈imaging width 70 μm). The wedge splitting tests were performed at a displacement rate of 0.05 mm min^{-1}. The SEM recording was set to 0.8 frames s^{-1}.

The crack tortuosity was measured on the recorded SEM images by image analysis using Fiji.[36] Given the high contrast between the fracture path and the rest of the microstructure, the crack can be thresholded and its profile can be analyzed with the plugin "skeletonize."[38] The skeleton of the fracture was pruned of any secondary branch and the length of the shortest longest path (*L*) was measured. The tortuosity τ was then calculated with the following expression (Equation (10))

$$\tau = \frac{L}{L_0} \tag{10}$$

with L_0 being the equivalent straight trajectory of the crack.

Quantification of the Sharpness in Covered Images: A series of pictures of a pattern with sharp black edges covered with a transparent sample

was collected using an optical microscope (Digital Microscope, Keyence VHX-5000, Keyence) to highlight the improvement in image sharpness that can be achieved by coupling a transparent nacre-like composite with a refractive index matching oil (Type B, immersion liquid, n_e = 1.518, Leica Microsystems GmbH, Germany). The specimen chosen has a relative interconnectivity χ/χ_0 of 1.13. Pictures of the pattern without the specimen, of the pattern with a mirror polished specimen placed in contact, and finally of the pattern with a specimen optically coupled through a refractive index matching oil were compared. Each image was analyzed by selecting over ten regions of interest per each image. Each region represents a strip of 600 µm in which there was a visible and sharp white-to-black color transition. Each strip was exported using the open source image analysis software Fiji[36] as a text image, the value of each cell being the gray value of each pixel. Every pixel column of the text image was therefore averaged and the standard deviation calculated, leading to averaged line scans displayed as pixel values as a function of the position in the image (in µm). Finally, each averaged line scan was stored and imported in MATLAB and fitted with a logistic function g through the line scan.[39] The logistic function has the following form (Equation (11))

$$g = \frac{M}{1 + \exp\left[-\kappa(x - x_0)\right]} \tag{11}$$

where M is the maximum pixel value of each line scan, κ is the steepness or logistic growth rate (expressed in mm^{-1}), and x_0 is the center position of the curve (expressed in mm).

Optical Properties: The optical characterization of the composites was performed using a V-660 UV–Vis spectrometer (Jasco Inc., USA) on specimens with a thickness of either 2.5 or 0.7 mm. To quantify the total diffuse transmittance of the specimens, the spectrometer was equipped with an integrating sphere (150 mm Integrating Sphere, Model ILV-924, Jasco Inc., USA). All spectra were collected in absorbance and normalized by the thickness of each specimen before conversion into the final transmittance values.

Supporting Information

Supporting Information is available from the Wiley Online Library or from the author.

Conflict of Interest

The authors declare no conflict of interest.

[1] F. Barthelat, *Bioinspiration Biomimetics* **2010**, *5*, 035001.
[2] U. G. K. Wegst, H. Bai, E. Saiz, A. P. Tomsia, R. O. Ritchie, *Nat. Mater.* **2015**, *14*, 23.
[3] M. E. Launey, M. J. Buehler, R. O. Ritchie, *Annu. Rev. Mater. Res.* **2010**, *40*, 25.
[4] H. D. Espinosa, J. E. Rim, F. Barthelat, M. J. Buehler, *Prog. Mater. Sci.* **2009**, *54*, 1059.
[5] R. Rabiei, S. Bekah, F. Barthelat, *Acta Biomater.* **2010**, *6*, 4081.
[6] F. Barthelat, R. Rabiei, *J. Mech. Phys. Solids* **2011**, *59*, 829.
[7] F. Barthelat, H. Tang, P. D. Zavattieri, C. Li, H. D. Espinosa, *J. Mech. Phys. Solids* **2007**, *55*, 306.
[8] B. L. Smith, T. E. Schäffer, M. Viani, J. B. Thompson, N. A. Frederick, J. Kindt, A. Belcher, G. D. Stucki, D. E. Morse, P. K. Hansma, *Nature* **1999**, *399*, 761.
[9] F. Barthelat, C. M. Li, C. Comi, H. D. Espinosa, *J. Mater. Res.* **2006**, *21*, 1977.
[10] K. S. Katti, D. R. Katti, S. M. Pradhan, A. Bhosle, *J. Mater. Res.* **2005**, *20*, 1097.
[11] H. D. Espinosa, A. L. Juster, F. J. Latourte, O. Y. Loh, D. Gregoire, P. Zavattieri, *Nat. Commun.* **2011**, *2*, 173.
[12] S. Deville, E. Saiz, R. K. Nalla, A. P. Tomsia, *Science* **2006**, *311*, 515.
[13] R. M. Erb, R. Libanori, N. Rothfuchs, A. R. Studart, *Science* **2012**, *335*, 199.
[14] S. Behr, U. Vainio, M. Müller, A. Schreyer, G. A. Schneider, *Sci. Rep.* **2015**, *5*, 9984.
[15] A. Walther, I. Bjurhager, J.-M. Malho, J. Pere, J. Ruokolainen, L. A. Berglund, O. Ikkala, *Nano Lett.* **2010**, *10*, 2742.
[16] I. Corni, T. J. Harvey, J. A. Wharton, K. R. Stokes, F. C. Walsh, R. J. K. Wood, *Bioinspiration Biomimetics* **2012**, *7*, 031001.
[17] H. Gao, S. Chen, L. Mao, Z. Song, H. Yao, H. Cölfen, X. Luo, F. Zhang, Z. Pan, Y. Meng, Y. Ni, S. Yu, *Nat. Commun.* **2017**, *8*, 287.
[18] V. Naglieri, B. Gludovatz, A. P. Tomsia, R. O. Ritchie, *Acta Mater.* **2015**, *98*, 141.
[19] H. Le Ferrand, F. Bouville, T. P. Niebel, A. R. Studart, *Nat. Mater.* **2015**, *14*, 1172.
[20] M. Grossman, F. Bouville, F. Erni, K. Masania, R. Libanori, A. R. Studart, *Adv. Mater.* **2017**, *29*, 1605039.
[21] F. Bouville, E. Maire, S. Meille, B. Van de Moortèle, A. J. Stevenson, S. Deville, *Nat. Mater.* **2014**, *13*, 508.
[22] G. X. Gu, F. Libonati, S. Wettermark, M. J. Buehler, *J. Mech. Behav. Biomed. Mater.* **2017**, *76*, 135.
[23] F. Song, A. K. Soh, Y. L. Bai, *Biomaterials* **2003**, *24*, 3623.
[24] K. Radi, D. Jauffres, S. Deville, C. L. Martin, *Composites, Part B* **2020**, *183*, 107699.
[25] T. Magrini, F. Bouville, A. Lauria, H. Le Ferrand, T. P. Niebel, A. R. Studart, *Nat. Commun.* **2019**, *10*, 2794.
[26] M. Grossman, F. Bouville, K. Masania, A. R. Studart, *Proc. Natl. Acad. Sci. USA* **2018**, *115*, 12698.
[27] T. P. Niebel, F. Bouville, D. Kokkinis, A. R. Studart, *J. Mech. Phys. Solids* **2016**, *96*, 133.
[28] L. J. Bonderer, A. R. Studart, L. J. Gauckler, *Science* **2008**, *319*, 1069.
[29] K. J. Koester, J. W. Ager, R. O. Ritchie, *Nat. Mater.* **2008**, *7*, 672.
[30] B. Cotterell, J. R. Rice, *Int. J. Fract.* **1980**, *16*, 155.
[31] R. O. Ritchie, *Nat. Mater.* **2011**, *10*, 817.
[32] L. Y. L. Wu, G. H. Tan, X. T. Zeng, T. H. Li, Z. Chen, *J. Sol-Gel Sci. Technol.* **2006**, *38*, 85.
[33] S. Martin, B. Bhushan, *J. Colloid Interface Sci.* **2017**, *488*, 118.
[34] X. Liu, Y. Xu, K. Ben, Z. Chen, Y. Wang, Z. Guan, *Appl. Surf. Sci.* **2015**, *339*, 94.
[35] E. Munch, M. E. Launey, D. H. Alsem, E. Saiz, A. P. Tomsia, R. O. Ritchie, *Science* **2008**, *322*, 1516.

[36] J. Schindelin, I. Arganda-Carreras, E. Frise, V. Kaynig, M. Longair, T. Pietzsch, S. Preibisch, C. Rueden, S. Saalfeld, B. Schmid, J. Tinevez, D. J. White, V. Hartenstein, K. Eliceiri, P. Tomancak, A. Cardona, *Nat. Methods* **2012**, *9*, 676.

[37] ASTM Standard E1820, *Standard Test Method for Measurement of Fracture Toughness*, ASTM International, West Conshohocken, PA **2013**.

[38] T.-C. Lee, R. L. Kashyap, *CVGIP: Graph. Models Image Process.* **1994**, *56*, 462.

[39] M. Gupta, J. Kaur, *IJARCCE* **2019**, *8*, 1.

[40] M. F. Ashby, in *Materials Selection in Mechanical Design* (Ed: F. A Michael), Butterworth Heinemann, Oxford, UK **2011**), Ch. 4.

2002149 (10 of 10)